Negative flat band magnetism in a spin– orbit-coupled correlated kagome magnet

Jia-Xin Yin[1,12], Songtian S. Zhang[1,12], Guoqing Chang[1,12], Qi Wang[2], Stepan S. Tsirkin[3], Zurab Guguchia[1,4], Biao Lian[5], Huibin Zhou[6,7], Kun Jiang[8], Ilya Belopolski[1], Nana Shumiya[1], Daniel Multer[1], Maksim Litskevich[1], Tyler A. Cochran[1], Hsin Lin[9], Ziqiang Wang[8], Titus Neupert[3], Shuang Jia[6,7], Hechang Lei[2] and M. Zahid Hasan[1,10,11]*

Electronic systems with flat bands are predicted to be a fertile ground for hosting emergent phenomena including unconventional magnetism and superconductivity[1–15], but materials that manifest this feature are rare. Here, we use scanning tunnel- ling microscopy to elucidate the atomically resolved electronic states and their magnetic response in the kagome magnet $Co_3Sn_2S_2$ (refs. [16–20]). We observe a pronounced peak at the Fermi level, which we identify as arising from the kinetically frustrated kagome flat band. On increasing the magnetic field up to ±8 T, this state exhibits an anomalous magnetization-polarized many-body Zeeman shift, dominated by an orbital moment that is opposite to the field direction. Such negative magnetism is induced by spin–orbit-coupling quantum phase effects[21–25] tied to non-trivial flat band systems. We image the flat band peak, resolve the associated negative magnetism and provide its connection to the Berry curvature field, show- ing that $Co_3Sn_2S_2$ is a rare example of a kagome magnet where the low-energy physics can be dominated by the spin–orbit-coupled flat band.

Exploring the interplay between symmetry-breaking order and electronic topology in a strong coupling setting[1–5] is emerging as a new frontier in fundamental physics, and not only helps develop new concepts related to phases of matter, but also provides indis- pensable knowledge to achieve future applications of quantum materials. The spin–orbit coupling effects in flat band systems have recently attracted significant interest as they exhibit strong inter-action and non-trivial topology, taking advantage of both[1–15]. Flat bands are rare and emerge only in a few systems such as twisted bilayer graphene, kagome lattices and heavy-fermion compounds. They can have two different origins: either they arise due to the lat- tice geometry as in the first two examples, or due to strongly local- ized atomic orbitals, as in the last example. Benefiting from the quenched kinetic energy, flat bands can host correlated electronic states including ferromagnetism, superconductivity and Wigner crystallization[8–11]. In the presence of spin–orbit coupling and time- reversal symmetry breaking, flat bands can further acquire a non- zero Chern number arising from a non-trivial Berry phase, with

the ability to support interacting topological phases including the fractional quantum Hall state[12–15]. Despite these exciting theoreti- cal prospects, experimental progress is halting, due to the scarcity of real materials with a flat band at the Fermi level and the chal- lenges in microscopically demonstrating the emergent behaviour in such systems.

Here we show the atomically resolved electronic structure of the kagome magnet $Co_3Sn_2S_2$ (refs. [16–20]) at 4.2 K under a tunable magnetic field with high-resolution scanning tunnelling micros- copy/spectroscopy (STM/S). We observe a pronounced peak at the Fermi level associated with the momentum-integrated state of the kagome flat band and discover a magnetization-polarized Zeeman effect. We theoretically study the relationship between the kagome flat band, the spin–orbit coupling effect, magnetism and the Berry curvature field on the magnetic ground state of this compound. All of our results and theoretical analysis taken together show that the dominant contribution of the orbital magnetism of the flat band originates from the Berry curvature field in $Co_3Sn_2S_2$, which in this particular case leads to a band-specific strong diamagnetism and other anomalous behaviour. Our work shows that $Co_3Sn_2S_2$ is a rare example of a kagome magnet where the low-energy physics can be dominated by the spin–orbit flat band.

$Co_3Sn_2S_2$ magnetic materials have been studied for quite som‒e time[16–20]. It has a layered crystal structure with the space group $R3\,m$ and hexagonal lattice constants a = 5.3 Å and c = 13.2 Å (Fig. 1a). It consists of a kagome Co_3Sn layer sandwiched between two hex- agonal S layers, which are further sandwiched between two hexago- nal Sn layers. The material has a ferromagnetic ground state (Curie temperature, T_C = 170 K) with the magnetization arising mainly from Co and aligned along the c axis[16]. The large electron nega- tivity difference leads to the strongest bonds forming between the Co and S atoms (Fig. 1b). On cleaving, the S–Sn bond is broken, yielding the S surface and the Sn surface (Fig. 1c). We observe atomic surface steps consistent with the expected height of c/3 (Fig. 1d), and we find two kinds of surface with the same hexagonal symme- try and lattice constant around a: one has a large corrugation with adatom defects (Fig. 1e), while the other has a smaller corrugation

[1]Laboratory for Topological Quantum Matter and Advanced Spectroscopy (B7), Department of Physics, Princeton University, Princeton, NJ, USA. [2]Department of Physics and Beijing Key Laboratory of Opto-electronic Functional Materials & Micro-nano Devices, Renmin University of China, Beijing, China. [3]Department of Physics, University of Zurich, Zurich, Switzerland. [4]Laboratory for Muon Spin Spectroscopy, Paul Scherrer Institute, Villigen PSI, Switzerland. [5]Princeton Center for Theoretical Science, Princeton University, Princeton, NJ, USA. [6]International Center for Quantum Materials and School of Physics, Peking University, Beijing, China. [7]CAS Center for Excellence in Topological Quantum Computation, University of Chinese Academy of Sciences, Beijing, China. [8]Department of Physics, Boston College, Chestnut Hill, MA, USA. [9]Institute of Physics, Academia Sinica, Taipei, Taiwan. [10]Materials Sciences Division, Lawrence Berkeley National Laboratory, Berkeley, CA, USA. [11]Princeton Institute for the Science and Technology of Materials, Princeton University, Princeton, NJ, USA. [12]These authors contributed equally: Jia-Xin Yin, Songtian S. Zhang, Guoqing Chang. *e-mail: mzhasan@princeton.edu

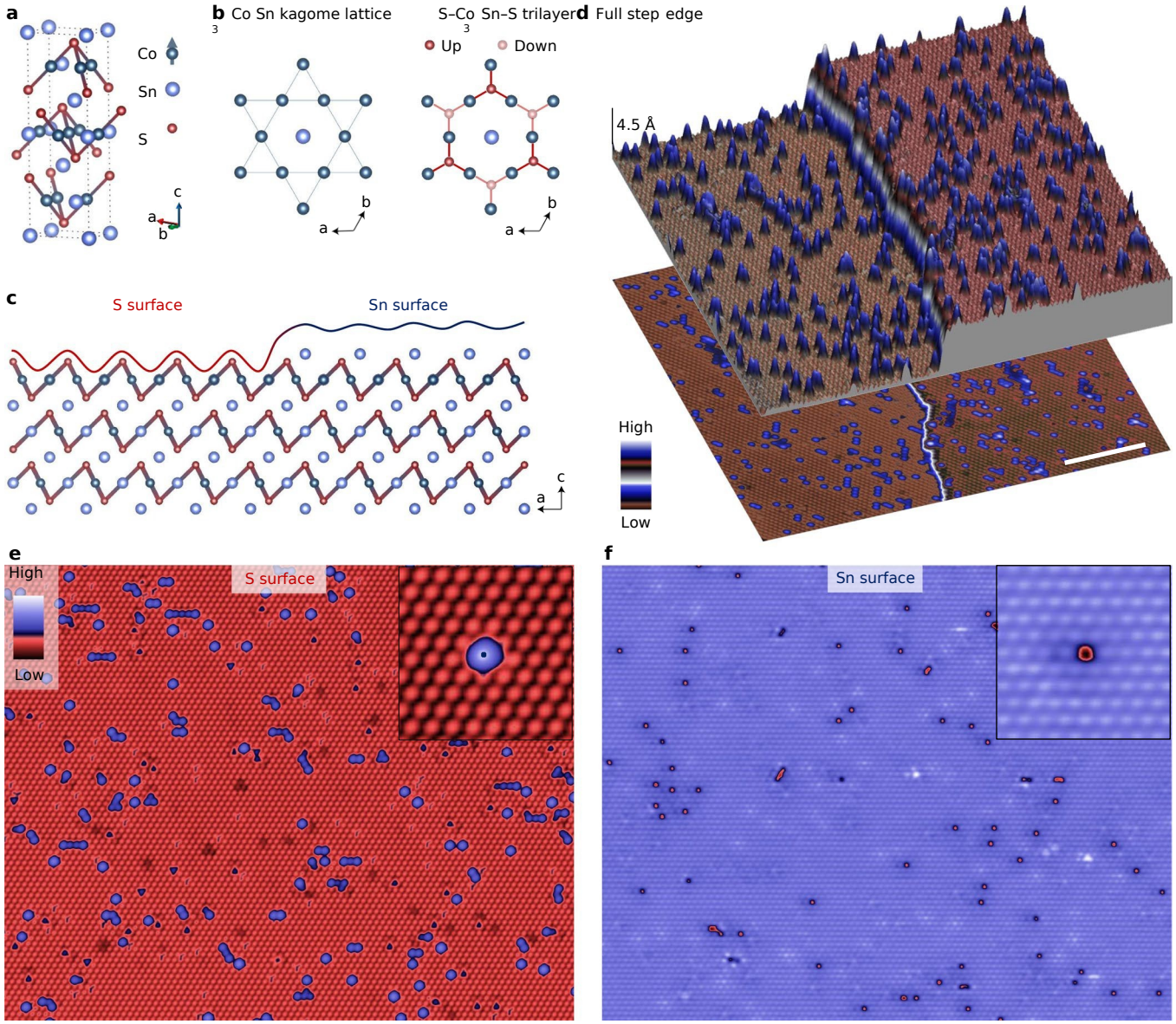

Fig. 1 | Atomic-scale visualization of the cleavage surface of $Co_3Sn_2S_2$. **a**, Crystal structure of $Co_3Sn_2S_2$. The crystal has a ferromagnetic ground state with spins on Co atoms aligned along the *c* axis. **b**, Kagome lattice structure of the Co_3Sn layer (left panel) and its bonding with the adjacent S layers (right panel). **c**, Side view of the crystal structure and illustration of the two possible terminating surfaces. The curve illustrates the surface profile. **d**, Topographic image of a full step between two surfaces of the same kind and its three-dimensional illustration. The step edge height is ~4.5 Å, consistent with *c*/3. **e**, Topographic image of the S surface. The inset shows the common defect (Sn adatom) on this surface, which sits at the hexagonal-close-packed site.
f, Topographic image of the Sn surface. The inset shows the common defect (Sn vacancy) on this surface.

with vacancy defects (Fig. 1f). As Sn has a larger atomic radius than S, the Sn surface can exhibit a smaller atomic corrugation (Fig. 1c). Moreover, since the Sn and S layers have a subatomic distance in the bulk, their bonding competes with the in-plane Sn–Sn bond. This competition can cause incomplete cleaving that creates Sn vacan- cies on the Sn surface and leaves Sn adatoms on the S surface. On the basis of their surface corrugations and atomic defects, we can identify these two surfaces as marked in Fig. 1e,f. Further conclu- sive evidence can be found by resolving the boundary between these two surfaces (Fig. 1c). Corroborating the previous identification, a representative topographic image (Fig. 2a) clearly demonstrates the coverage of the Sn adatoms gradually increasing on the S surface, eventually forming an atomically flat Sn surface.

Having identified these two surfaces at the atomic scale, we characterize their electronic structure by measuring the differential

conductance on the clean areas (Fig. 2b). We find that the spectrum on the S surface exhibits a sharp peak at $E_P = -8$ meV with more states below E_F (Fermi energy), whereas the Sn surface has more states above E_F and no detectable peak. These spectral features are reproducibly observed on different samples. Notably, the sharp peak does not shift with increasing temperature up to 45 K (Fig. 2b inset), nor is there any enhanced scattering vector at this energy when we analyse the spectroscopic map over a large S surface by Fourier transform (Fig. 2d). These observations exclude a simple charge or magnetic order origin of this state (for example, as a coherent peak of an asymmetric energy gap), which often exhibits a strong tem- perature-dependent evolution in energy as well as a well-defined wavevector in the quasi-particle scattering channel. Moreover, as the sharp peak is present on only one surface, whether it is a surface state or a projection of the bulk state needs be determined.

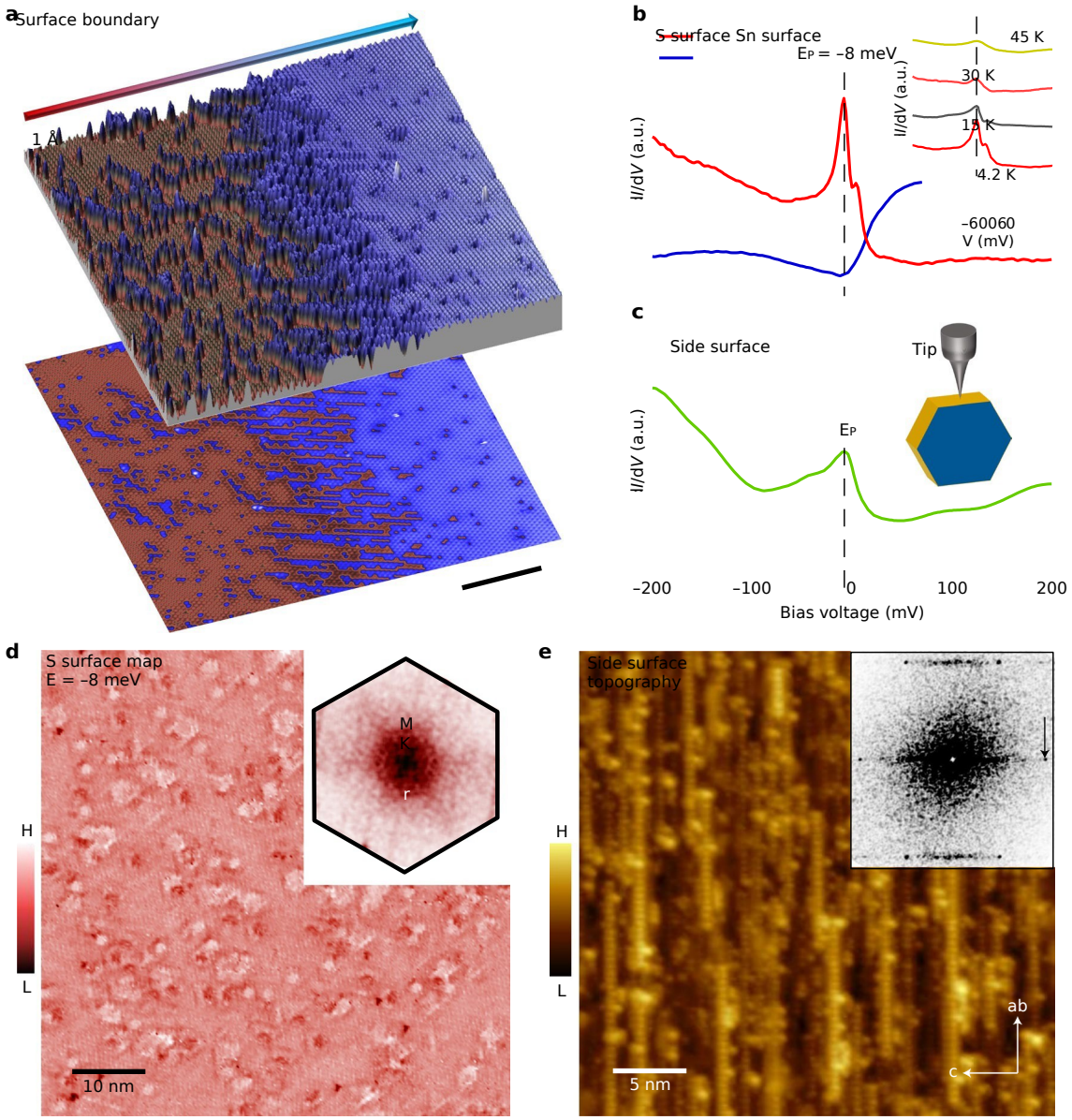

Fig. 2 | Observation of a sharp peak around the Fermi energy. **a**, Surface boundary between the Sn surface and the S surface and the three-dimensional view. The S surface smoothly evolves to become the Sn surface with the increased coverage of Sn adatoms. **b**, Differential conductance spectrum taken on S (red) and Sn (blue) surfaces away from any defects. Inset: temperature evolution of the spectrum taken on the S surface. **c**, Averaged spectrum taken on the side cleaving surface. Inset: illustration of the tunnelling geometry. **d**, Differential conductance map on the S surface at $E = -8$ meV. Inset: Fourier transform image. **e**, Topographic image of the side surface showing a stripe-like atomic structure. Inset: a Fourier transform image, where the arrow marks the Bragg peak corresponding to $(c/3)^{-1}$.

To address this question experimentally, we designed a clamp sample holder to allow us to perform side cleaving and tunnel to the side surface with atomic precision, which would produce a surface environment different from the above two surfaces. Through multiple trials on a large number of samples, we were able to obtain a surface with quasi-atomic lattice structure (Fig. 2e) and detectable Bragg peaks in its Fourier transform image (Fig. 2e inset). Notably, we observe a broader peak on this surface (Fig. 2c), located at the same energy as the sharp peak observed on the S surface despite the large difference in their surface environments. This observa- tion indicates that this state is more likely to be an intrinsic band structure feature.

To examine the band structure origin of this peak, we per- form first-principles calculations on its electronic structure. The

calculated orbital-resolved local density of states (LDOS) for the Sn-terminated surface, the S-terminated surface and the bulk are shown in Fig. 3a, respectively. In all cases, the Co 3*d* orbital is always the strongest, which agrees with the general consensus that the low- energy physics of transition metal-based materials are often domi- nated by the 3*d* electrons[26]. For the two surface cases, there exists a noticeable peak at low energy only for the S-terminated surface as shown in the upper and middle panels of Fig. 3a. The remarkable surface-resolved spectroscopic consistency with our STM measure- ments in Fig. 2 confirms the validity of both experiment and calcu- lation. We also find that the bulk states feature this peak as shown in the lower panel of Fig. 3a, in support of the interpretation that the experimentally observed peak stems from the bulk band. Crucially, the calculation also provides momentum space insight into the

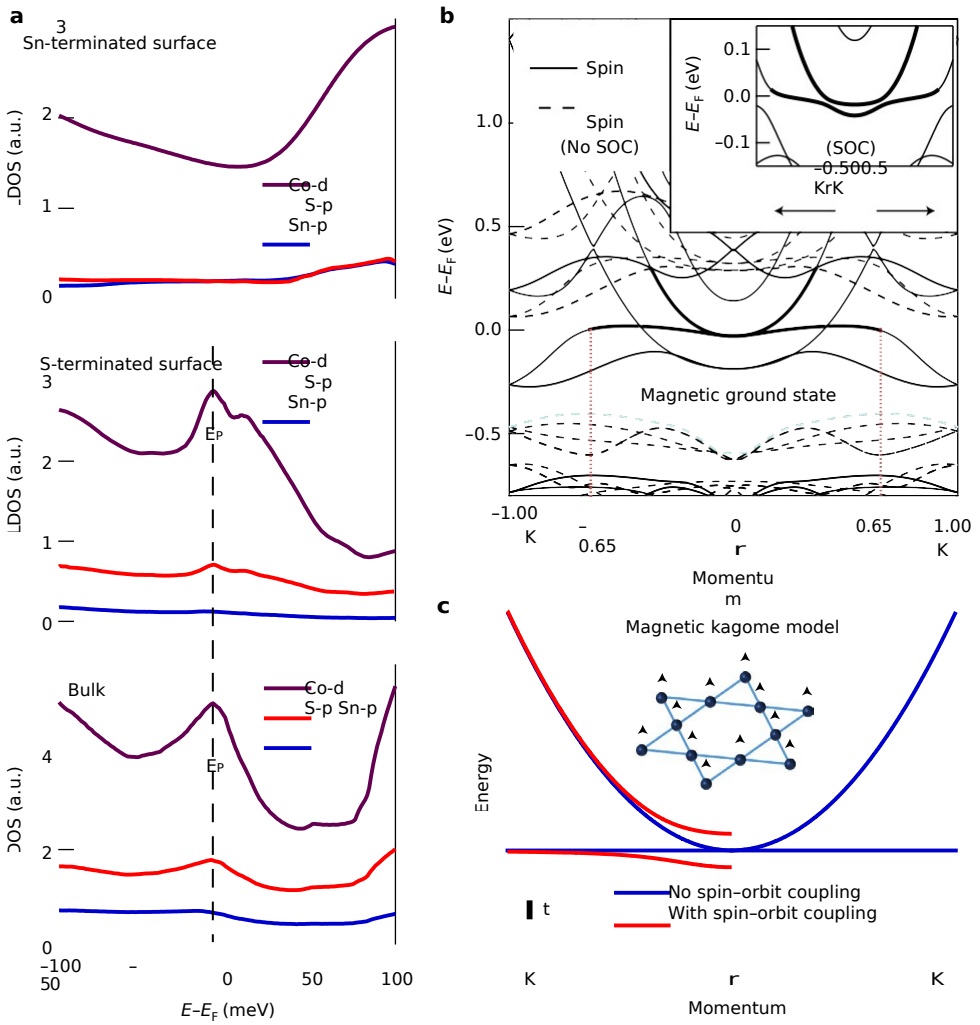

Fig. 3 | Magnetic kagome flat band nature of the density-of-state peak. **a**, Calculated LDOS on the Co (within the Co_3Sn layer), S (within the S layer) and Sn (within the Sn layer) atoms at the Sn-terminated surface (upper panel) and S-terminated surface (middle panel), respectively. Lower panel: calculated DOS on the Co, S and Sn atoms in the bulk. All of the above calculations include spin–orbit coupling. **b**, Calculated spin-resolved band structure without spin–orbit coupling at $k_z = 0$, showing a nearly flat band degenerate with an electron-like band bottom near the Fermi level. With spin–orbit coupling included, there is a further hybridization between these two bands (inset), and their accumulated states contribute to the LDOS peak at E_F. **c**, Tight-binding model of a single-layer magnetic kagome with (red) and without (blue) spin–orbit coupling (coupling strength $\lambda = 0.2t$, where t is the nearest-neighbour hopping integral). The inset illustrates the kagome lattice with ferromagnetism.

origin of this peak, in that it arises from a nearly flat band that hybridizes with an electron-like band bottom due to spin–orbit coupling as shown in Fig. 3b and its inset. Consistent with previ- ous bulk calculations identifying this material as a half-metallic fer- romaget[17–20], the low-energy states around the Fermi energy are all spin-majority states (Fig. 3b).

We find that the essential momentum features of the flat band can be captured by the fundamental kagome model (Fig. 3c). A tight-binding model for nearest-neighbour hopping on the kagome lattice gives a kinetically frustrated flat band degenerate with a qua- dratically dispersing band at the origin of reciprocal space. The intrinsic breaking of time-reversal symmetry splits the spin-degen- erate bands into two sets well separated in energy. Spin–orbit cou- pling further lifts the band degeneracy at the Γ point and makes the originally flat band weakly dispersive. In this model, the flat band has a non-trivial Chern number carrying Berry phase effects[21–25].

As the peak on the S surface is the sharpest spectroscopic feature of the tunnelling signal and has its origin in the kagome flat band, we explore the spin–orbit-related Berry phase effects by applying a strong magnetic field and performing spectroscopic measurements

with high spatial and energy resolution. The *c*-axis field-dependent measurement at the same atomic site reveals that the peak shifts progressively to higher energies with increasing field magnitude independent of whether the field is parallel or antiparallel to the *c* axis (Fig. 4a,b). Fitting the field evolution of this shift with a linear function yields a slope of 0.17 ± 0.01 meVT^{-1} = 2.9 ± 0.2 μ_B (Fig. 4e). Moreover, the energy shift $\Delta E_{8\text{-}0\ T}$ over a clean S area is spatially homogeneous with an average value of 1.4 meV (Fig. 4c,d), from which an average magnitude of the magnetic moment 3.0 ± 0.3 μ_B can be derived from our data (Fig. 4f). The observed field-induced shift of the flat band peak in this kagome magnet is unusual and unprecedented in the literature as we discuss below.

In a spin doubly degenerate system, an applied magnetic field splits a density-of-states peak into two peaks separated in energy, as in the conventional Zeeman effect often seen in tunnelling experiments[27]. In the spin singly degenerate case, the magnetic field will instead only shift the state in energy, the sign of which depends on the respective field orientation. When the magnetic moment of the state is polarized with an applied field in the presence of the fer- romagnetic order, the state will always shift to the same direction

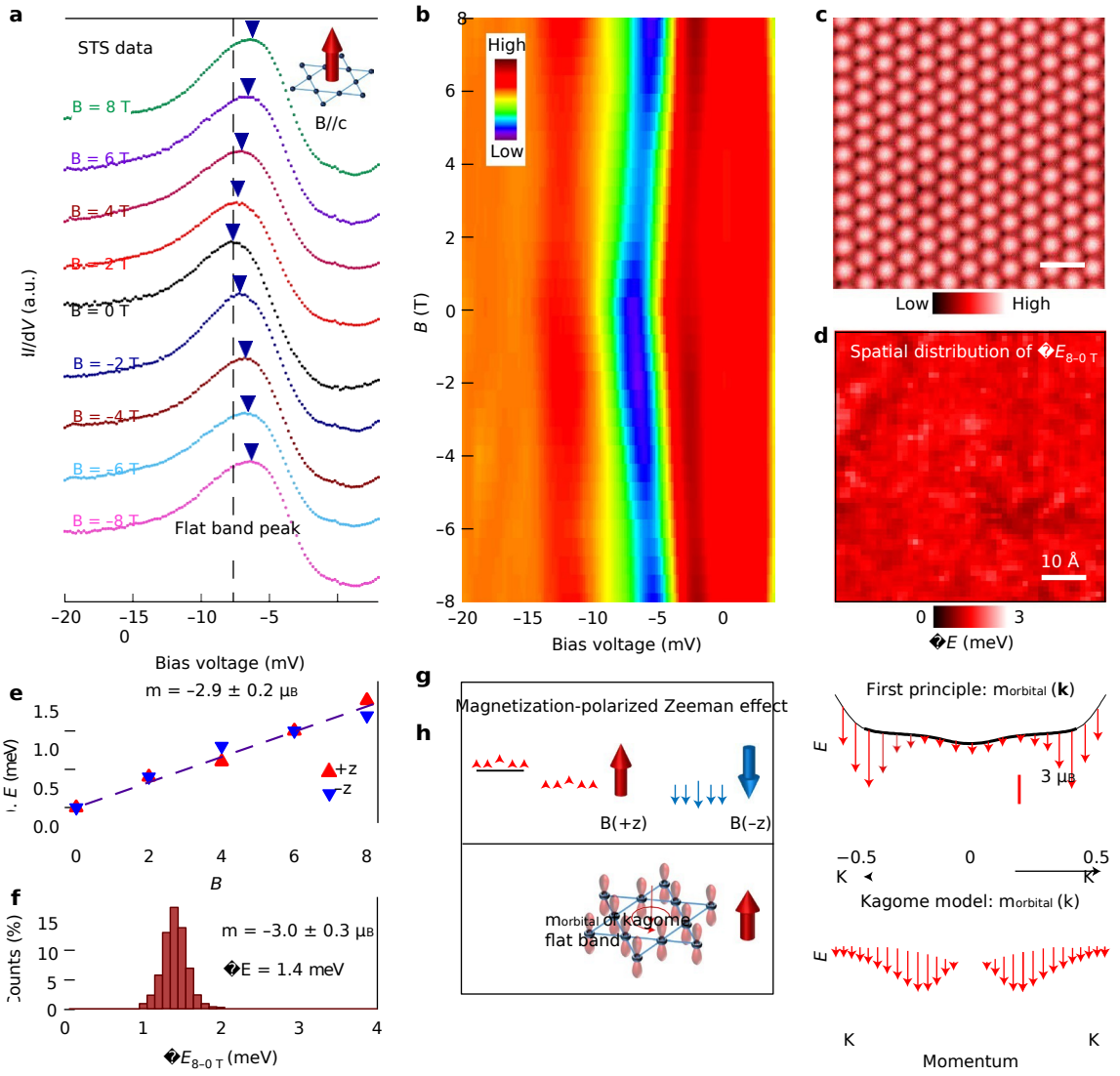

Fig. 4 | Negative orbital magnetism of the flat band peak. **a**, Magnetic field dependence of the peak on the S surface. The peak exhibits a shift in energy of equal magnitude with the field applied in either *c* axis direction. The inset illustrates the magnetic field perpendicular to the kagome lattice. **b**, Intensity plot of the second derivative of the interpolated field-dependent tunnelling spectra, showing a similar shift as in **a**. **c**, Topographic image of a clean S surface. **d**, Energy-shift map between 8 T and 0 T for this surface. **e**, Energy-shift of peak as a function of external field, from which the magnetic moment value can be derived as $m = -2.9 \pm 0.2\ \mu_B$. The error bars denote energy resolution. **f**, Histogram of the energy-shift over the area in **c** and **d**, showing an average value of 1.4 meV that gives $m = -3.0 \pm 0.3\ \mu_B$. **g**, Upper panel: illustration of the magnetization-polarized Zeeman effect. The applied field aligns the spins in the same orientation and the energy shift is the same for field applied in both orientations (see Supplementary Information for further elaboration).
Lower panel: illustration of the large negative orbital magnetism of the flat band in the kagome lattice. **h**, Upper panel: orbital magnetism for the flat band calculated from first principles (full band structure shown in Fig. 3b). The magnetic moment (red arrows) is plotted along the flat band. The red bar marks the units of the magnetic moment value. Lower panel: orbital magnetism from the magnetic kagome lattice model. The magnetic moment (red arrows, arbitrary unit) is plotted along the flat band.

in energy regardless of the relative field orientation (Fig. 4g upper panel, see Supplementary Information for further elaboration). The systematic data trend we see (Fig. 4a–f) suggests a magnetization- polarized scenario. If the magnetic moment has the same sign as the field, its energy should be lowered (Fig. 4g upper panel). Our measurements instead clearly show this peak shifting towards posi- tive energies, indicating an effective negative magnetic moment of the state. Such a negative magnetic moment ($-3\ \mu_B$) is highly non-trivial, as the conventional magnetization-polarized spin

existence of spin–orbit coupling in the kagome flat band (lower panel in Fig. 4g).

Our first-principles calculation reveals the existence of orbital magnetism associated with the flat band with negative sign as shown in the upper panel of Fig. 4h (diamagnetic in this specific band, while the sample as a whole is ferromagnetic). This negative sign is in agreement with our experimental results. In the magnetic kagome model, we find that $m_{\mathrm{orbital}}(\mathbf{k})$ for the flat band computed analytically within a **k·p** approximation is proportional to

contribution is positive with a much smaller magnitude of ≈1 μ_B. This contrast indicates that there are orbital contributions in the magnetic response beyond the spin Zeeman effect. Considering the non-trivial Berry phase of the flat band, it is likely that there exists a negative orbital magnetic moment resulting from the $\frac{\mathbf{k}^2 t^2 \lambda}{\mathbf{k}^4 t^2 + 48\lambda^2}$ as shown in the lower panel of Fig. 4h, where λ is the spin–orbit coupling strength and t is the nearest-neighbour hop- ping integral. This offers a heuristic reference for understanding the negative orbital magnetism tied to the sign of the microscopic

spin–orbit coupling, which also determines the sign of the Berry curvature. Since the spin–orbit coupling term is proportional to $L \cdot S$, this orbital magnetic moment is also tied to the spin magnetization polarized by the applied magnetic field. Thus, the associ-ated field-driven energy shift follows the magnetization-polarized scenario depicted in Fig. 4g. As there can also be electron–electron interaction for 3*d* orbitals involving multiple bands, a complete and quantitative understanding of this emergent behaviour requires a comprehensive quantum many- body theory of correlated electrons on the kagome lattice with strong magnetic polarization and spin–orbit coupling. Crucially, the orbital magnetism of the flat band is a generic property of the kagome lattice in the ferromagnetic state with spin–orbit coupling, and can therefore be generally applied to a large family of transition metal-based kagome materials, whose electronic structures are of recent interest[7,28,29]. In our study, we do not find unambiguous evidence for Weyl nodes in the electronic structure. However, our observation of a sharp peak located just below the Fermi level with strong Berry phase effects also indi-cates that the nearby flat band can contribute substantially to the anomalous low-energy physics, and therefore be probed readily in transport. Our methodology of probing band- resolved ordering phenomena such as spin–orbit magnetism[21– 25,30] can also be applied in future experiments to elucidate other exotic phenomena includ-ing flat band superconductivity and anomalous quantum transport. An experimental handle on these effects in exploring quantum materials in general is a crucial milestone in the field of strong correlation and quantum topology.

references

1. Soumyanarayanan, A., Reyren, N., Fert, A. & Panagopoulos, C. Emergent phenomena induced by spin–orbit coupling at surfaces and interfaces. *Nature* **539**, 509–517 (2016).
2. Wang, J. & Zhang, S.-C. Topological states of condensed matter. *Nat. Mater.* **16**, 1062–1067 (2017).
3. Hasan, M. Z., Xu, S.-Y. & Bian, G. Topological insulators, topological superconductors and Weyl fermion semimetals. *Phys. Scr.* **T164**, 014001 (2015).
4. Hasan, M. Z., Xu, S.-Y., Belopolski, I. & Huang, S.-M. Discovery of Weyl fermion semimetals and topological Fermi arc states. *Annu. Rev. Condens. Matter Phys.* **8**, 289–309 (2017).
5. Sachdev, S. Topological order, emergent gauge fields, and Fermi surface reconstruction. *Rep. Prog. Phys.* **82**, 014001 (2019).
6. Cao, Y. et al. Unconventional superconductivity in magic-angle graphene superlattices. *Nature* **556**, 43–50 (2018).
7. Yin, J.-X. et al. Giant and anisotropic spin–orbit tunability in a strongly correlated kagome magnet. *Nature* **562**, 91–95 (2018).
8. Belopolski, I. et al. Topological Weyl lines and drumhead surface states in a room-temperature magnet. Preprint at https://arxiv.org/abs/1712.09992 (2017).
9. Si, Q. & Steglich, F. Heavy fermions and quantum phase transitions. *Science* **329**, 1161–1166 (2010).
10. Mielke, A. Exact ground states for the Hubbard model on the Kagome lattice. *J. Phys. Rev. Lett.* **69**, 1608 (1992).
11. Wu, C., Bergan, D., Balents, L. & Sarma, S. D. Flat bands and Wigner crystallization in the honeycomb optical lattice. *Phys. Rev. Lett.* **99**, 070401 (2007).
12. Leykam, D., Andreanov, A. & Flach, S. Artificial flat band systems: from lattice models to experiments. *Adv. Phys. X* **3**, 1473052 (2018).
13. Tang, E., Mei, J. W. & Wen, X. G. High-temperature fractional quantum Hall states. *Phys. Rev. Lett.* **106**, 236802 (2011).
14. Sun, K. et al. Nearly flat bands with nontrivial topology. *Phys. Rev. Lett.* **106**, 236803 (2011).
15. Neupert, T. et al. Fractional quantum Hall states at zero magnetic field. *Phys. Rev. Lett.* **106**, 236804 (2011).
16. Vaqueiro, P. & Sobany, G. G. A powder neutron diffraction study of the metallic ferromagnet $Co_3Sn_2S_2$. *Solid State Sci.* **11**, 513–518 (2009).

17. Dedkov, Y. S., Holder, M., Molodtsov, S. L. & Rosner, H. Electronic structure of shandite $Co_3Sn_2S_2$. *J. Phys. Conf. Ser.* **100**, 072011 (2008).
18. Schnelle, W. et al. Ferromagnetic ordering and half-metallic state of $Sn_2Co_3S_2$ with the Shandite-type structure. *Phys. Rev. B* **88**, 144404 (2013).
19. Wang, Qi et al. Large intrinsic anomalous Hall effect in half-metallic ferromagnet $Co_3Sn_2S_2$ with magnetic Weyl fermions. *Nat. Commun.* **9**, 3681 (2018).
20. Liu, E. et al. Giant anomalous Hall angle in a half-metallic magnetic Weyl semimetal. *Nat. Phys.* **14**, 1125–1131 (2018).
21. Karplus, R. & Luttinger, J. M. Hall effect in ferromagnetics. *Phys. Rev.* **95**, 1154–1160 (1954).
22. Xiao, D., Chang, M. C. & Niu, Q. Berry phase effects on electronic properties. *Rev. Mod. Phys.* **82**, 1959–2007 (2010).
23. Resta, R. Electrical polarization and orbital magnetization: the modern theories. *J. Phys. Condens. Matter* **22**, 123201 (2010).
24. Thonhauser, T. Theory of orbital magnetization in solids. *Int. J. Mod. Phys. B* **25**, 1429 (2011).
25. Vanderbilt, D. *Berry Phases in Electronic Structure Theory: Electric Polarization, Orbital Magnetization and Topological Insulators* (Cambridge University Press, Cambridge, 2018).
26. Fischer, Ø. et al. Scanning tunneling spectroscopy of high-temperature superconductors. *Rev. Mod. Phys.* **79**, 353 (2007).
27. Ternes, M., Heinrich, Andreas., J. & Schneider, W.-D. Spectroscopic manifestations of the Kondo effect on single adatoms. *J. Phys. Condens. Matter* **21**, 053001 (2009).
28. Nayak, A. K. et al. Large anomalous Hall effect driven by a nonvanishing Berry curvature in the noncolinear antiferromagnet Mn_3Ge. *Sci. Adv.* **2**, e1501870 (2016).
29. Kuroda, K. et al. Evidence for magnetic Weyl fermions in a correlated metal. *Nat. Mater.* **16**, 1090–1095 (2017).
30. Aivazian, G. et al. Magnetic control of valley pseudospin in monolayer WSe_2. *Nat. Phys.* **11**, 148–152 (2015).

Acknowledgements

STM experimental and theoretical work at Princeton University was supported by the Gordon and Betty Moore Foundation (GBMF4547/M.Z.H.). ARPES characterization of the sample is supported by the United States Department of Energy (US DOE) under the Basic Energy Sciences programme (grant number DOE/BES DE-FG-02–05ER46200).
Work at Renmin University was supported by the Ministry of Science and Technology of China (2016YFA0300504), the National Natural Science Foundation of China (nos. 11574394, 11774423 and 11822412), the Fundamental Research Funds for the Central Universities, and the Research Funds of Renmin University of China (15XNLF06, 15XNLQ07 and 18XNLG14). S.S.T. and T.N. acknowledge support from the European Union's Horizon 2020 research and innovation programme (ERC-StG-Neupert-757867-PARATOP). Z.W. and K.J. acknowledge US DOE grant DE-FG02– 99ER45747. We also acknowledge the Natural Science Foundation of China (grant nos. 11790313 and 11774007), the Key Research Program of the Chinese Academy of Sciences (grant no. XDPB08-1), the National Key R&D Program of China (grant nos. 2016YFA0300403 and 2018YFA035601), the Princeton Center for Theoretical Science and the Princeton Institute for the Science and Technology of Materials Imaging and Analysis Center at Princeton University. Muon spin rotation (μSR) experiments were performed at the πE3 beamline of the Paul Scherrer Institute, using the HAL-9500 μSR spectrometer. Z.G. acknowledges R. Scheuermann for support in the μSR experiments.
M.Z.H. acknowledges support from Lawrence Berkeley National Laboratory and the Miller Institute of Basic Research in Science at the University of California, Berkeley in the form of a Visiting Miller Professorship.

Author contributions

J.-X.Y. and S.S.Z. conducted the STM and STS experiments in consultation with M.Z.H.; Q.W., H.Lei, H.Z. and S.J. synthesized and characterized the sequence of samples; Z.G. performed μSR measurements in consultation with M.Z.H.; G.C., T.N., S.S.T., B.L., K.J., H.Lin and Z.W. carried out theoretical analysis in consultation with J.-X.Y. and M.Z.H.; I.B., N.S., D.M., M.L. and T.A.C. contributed to sample characterization and instrument calibration; J.-X.Y., S.S.Z. and M.Z.H. performed the data analysis and figure development and wrote the paper with contributions from all authors; M.Z.H. supervised the project. All authors discussed the results, interpretation and conclusion.

Competing interests

The authors declare no competing interests.

Additional information

Correspondence and requests for materials should be addressed to M.Z.H.

Journal peer review information: Nature Physics thanks Oleg Yazyev and other anonymous reviewer(s) for their contribution to the peer review of this work.

Methods

Single crystals of $Co_3S_2Sn_2$ up to 1.5 mm × 1.5 mm × 0.3 mm were used in this study. More than 30 samples were cleaved mechanically in situ at 77 K in ultrahigh-vacuum conditions, and then immediately inserted into the STM head, already at He4 base temperature. The magnetic field was applied under zero-field cooling, after which we carefully approached the tip to locate the same atomic-scale area for tunnelling spectroscopy. We also carefully calibrated zero energy using a 'zero-current, zero-voltage' technique for different fields. Tunnelling conductance spectra were obtained with Ir/Pt tips using standard lock-in amplifier techniques with a root-mean-square oscillation voltage of 1 meV–0.2 meV and a lock-in frequency of 973 Hz. The topographic images were taken with the tunnelling junction set-up: $V = -50$ mV, $I = 200$ pA; the conductance maps were taken with the tunnelling junction set-up: $V = -50$ mV, $I = 200$ pA and $V = -15$ mV, $I = 300$ pA; and the tunnelling spectra were taken with the junction set-up: $V = -200$ mV, $I = 1$ nA and $V = -20$ mV, $I = 0.5$ nA.

Data availability

The data that support the plots within this paper and other findings of this study are available from the corresponding author upon reasonable request.